Aerosol Effects on Simulated Storm Electrification and Precipitation in a Two-Moment Bulk Microphysics Model

EDWARD R. MANSELL AND CONRAD L. ZIEGLER

NOAA/National Severe Storms Laboratory, Norman, Oklahoma

ABSTRACT

The effects of cloud condensation nuclei (CCN) concentrations are found to strongly affect the microphysical and electrical evolution of a numerically simulated small multicell storm. The simulations reproduce the well-known effects of updraft invigoration and delay of precipitation formation as increasing CCN from low to intermediate concentrations causes droplet sizes to decrease. Peak updrafts increased from $16 \, \mathrm{m \, s^{-1}}$ at the lowest CCN to a maximum of 21–$22 \, \mathrm{m \, s^{-1}}$ at moderate CCN, where condensation latent heating is maximized. The transition from low to high CCN first maximizes warm-rain production before switching over to the ice process as the dominant precipitation mechanism. Average graupel density stays fairly high and constant at lower CCN, but then drops monotonically at higher CCN concentration, although high CCN also foster the appearance of small regions of larger, high-density graupel with high simulated radar reflectivity.

Graupel production increases monotonically as CCN concentration rises from 50 to about $2000 \, \mathrm{cm^{-3}}$. The lightning response is relatively weak until the Hallett–Mossop rime-splintering ice multiplication becomes more active at CCN $> 700 \, \mathrm{cm^{-3}}$. At very high CCN concentrations ($>2000 \, \mathrm{cm^{-3}}$), graupel production decreases slowly, but lightning activity drops dramatically when the parameterization of Hallett–Mossop rime-splintering ice multiplication is based on the number of large cloud droplets collected by graupel. Conversely, lightning activity remains steady at extremely high CCN concentration when the Hallett–Mossop parameterization is based simply on the rate of rime mass accumulation. The results lend support to the aerosol hypothesis as applied to lightning production, whereby greater CCN concentration tends to lead to greater lightning activity, but with a large sensitivity to ice multiplication.

1. Introduction

The general effects of the concentration of cloud condensation nuclei (CCN) on cloud microphysics are reasonably well understood [e.g., review article by Tao et al. (2012)], although the tandem impact of CCN on the precipitation and electrification processes in convective storms has been less explored with cloud models. In the present study, the effects of varying CCN concentration on the microphysics and electrification of a small multicell storm are simulated with a three-dimensional cloud model. Previous cloud simulation studies involving CCN effects on electrification using explicit charging parameterizations have been limited to the axisymmetric Takahashi (1984) and 1D Mitzeva et al. (2006) models. Those two studies only tested two

values of CCN concentration to represent maritime and continental conditions, so no transition details could be studied, but they did show significant differences between low and high CCN. Nonelectrical model studies have also shown dramatic changes in precipitation for different CCN concentrations (e.g., Khain and Pokrovsky 2004; Wang 2005; Seifert and Beheng 2006; Li et al. 2008). Although Khain et al. (2008) did not include explicit electrification processes, their results showed a potentially significant effect of aerosols on the main ingredients for electrification: graupel, small ice particles, and supercooled liquid droplets.

Precipitation in convective storms develops via some combination of warm- and cold-cloud processes (e.g., Rogers and Yau 1989). The warm-cloud process is dominated by the combined effects of condensation and quasi-stochastic drop coalescence (i.e., binary coalescence or self-collection of cloud droplets to form drizzle-sized raindrops, followed by rain collection of cloud and rain self-collection). The cold-cloud process is initiated mainly by production of graupel embryos via 1) drop freezing

Corresponding author address: Edward R. Mansell, National Severe Storms Laboratory, 120 David L. Boren Blvd., Norman, OK 73072.
E-mail: ted.mansell@noaa.gov

and 2) riming of vapor-grown and aggregated snow particles. Subsequent precipitation growth is dominated by graupel riming of cloud. Rain can be predominantly produced from graupel meltwater in mixed-phase storms.

The CCN concentration has the capacity to modulate the warm- and cold-cloud processes in several ways. For example, lower CCN concentration promotes faster droplet growth because of reduced competition for water vapor. Larger droplets increase the coalescence rate and accelerate the growth of raindrops. Conversely, high CCN concentration forces high concentrations of smaller droplets, making coalescence less efficient and delaying or even suppressing warm-rain formation. Droplet size (along with other factors) also affects the density of rime [see Eq. (A2)] acquired by graupel in dry-growth mode (i.e., surface temperature $T_s < 0°C$), with smaller drops resulting in lower rime density and larger drops promoting higher-density growth. Frozen-drop graupel embryo formation is regulated by the median volume size of coalesced drops such that smaller raindrops do not freeze until lower temperatures are reached.

The impact of CCN on convective storm evolution has been the subject of several numerical cloud modeling studies. Khain et al. (1999) and Khain et al. (2005) presented results from spectral bin microphysics, finding that increasing aerosol concentration delayed the formation of raindrops and allowed more droplets to attain subfreezing temperatures and produce greater ice contents aloft. Wang (2005) examined aerosol effects in a tropical squall line over a wide range of CCN concentrations with two-moment bulk microphysics, finding that increasing aerosols generally invigorated the convection and increased total rainfall. Li et al. (2008) employed a two-moment bulk microphysics scheme and found that precipitation in a simulated Texas Gulf Coast storm increased with increasing CCN concentration from low to moderately high values as a result of reduced warm-rain coalescence leading to enhancement of the mixed-phase precipitation process. At extremely high CCN, Li et al. (2008) noted reduced accumulated precipitation to the point of full suppression, which agrees with satellite-based observations of clouds in clear and smoke-filled air (Rosenfeld 1999). The study by van den Heever and Cotton (2007) demonstrated that simulated storm dynamics were sensitive to suppression of the warm-rain process caused by CCN enhancement, thereby exerting a strong influence on precipitation. Fan et al. (2009) focused on aerosol effects in environments with various wind shear and humidity profiles using bin microphysics in a two-dimensional framework, concluding that invigoration was more effective in weaker shear and that increased aerosols tended to reduce precipitation rates in stronger shear. In a high–wind shear environment

with two-moment microphysics, Storer et al. (2010) compared simulations with varying aerosol concentrations and convective available potential energy (CAPE) and also noted lower precipitation for higher CCN at moderate to high shear, but a lesser effect at lower shear.

Charge separation between rebounding collisions between ice particles in the presence of supercooled droplets is widely recognized as the primary electrification mechanism in storms via laboratory studies (e.g., Reynolds et al. 1957; Takahashi 1978) and aircraft observations (e.g., Dye et al. 1986). Numerical simulations have also supported the role of graupel–ice collisions in electrification (e.g., Takahashi 1983; Helsdon et al. 2001, 2002; Mansell et al. 2005). Storm electrification is therefore highly sensitive to production of ice particles, as well as to supercooled liquid droplets. CCN aerosol effects have been suspected to play a significant role in differences of lightning production between maritime and continental thunderstorms, but the convolution of aerosol and thermodynamic differences over land and sea have left ambiguities in observational evidence, with nonaerosol factors perhaps playing the primary role (e.g., Williams et al. 2002; Williams and Stanfill 2002). Yuan et al. (2011) and Yuan et al. (2012) presented satellite-based evidence for lightning enhancement in the presence of increased aerosol loading by volcanic activity without any obvious changes in the meteorology (e.g., thermodynamic and moisture profiles), providing support for the hypothesis that oceanic convection could produce more lightning if more CCN aerosols were present.

The present study revisits the sensitivity to CCN concentration noted by Mansell et al. (2010) in a case study of microphysical and electrical evolution in a small Oklahoma thunderstorm that was observed on 29 June 2004 during the Thunderstorm Electrification and Lightning Experiment (TELEX) (MacGorman et al. 2008; Bruning et al. 2007). That case appeared to be a suitable test bed for exploring some aspects of the aerosol hypothesis for electrification, which broadly proposes an importance of aerosol effects to microphysics and therefore electrification. Anecdotal evidence of urban aerosol effects on lightning (e.g., Orville et al. 2001; Steiger and Orville 2003; Naccarato et al. 2003) is complicated by the presence of heat island effects (van den Heever and Cotton 2007). The effects of anthropogenic aerosols on rainfall have also been the subject of conflicting results (e.g., Schultz et al. 2007).

Very few previous simulation studies of CCN effects have been performed using explicit electrification. Takahashi (1984) used spectral bin microphysics in an axisymmetric dynamic model to compare maritime (low) CCN and continental (high) CCN in a no-shear, cold-season environment and noted significant enhancement

of electrification for the continental CCN. Takahashi (1984) concluded that aerosols might be responsible for differences in electrification between the maritime and continental regimes, but mainly as an effect of forcing graupel to charge more consistently to generate a strong dipole charge, and not necessarily as an effect of invigoration or greater ice production. The 1D model simulation results of Mitzeva et al. (2006) with a single-moment bulk microphysics scheme found updraft enhancement, greater ice production, and stronger electrification with continental aerosol content compared to maritime. The present study expands on this previous work by testing a wide range of CCN concentrations in a 3D model with sufficiently sophisticated two-moment bulk microphysics for physically realistic responses.

2. Cloud model

a. Numerics

This study used the Collaborative Model for Multiscale Atmospheric Simulation (COMMAS) (Mansell et al. 2010; Wicker and Wilhelmson 1995). The model uses the basic equation set from Klemp and Wilhelmson (1978) for momentum, pressure, potential temperature, and turbulent kinetic energy. Time integration is performed with a third-order Runge–Kutta scheme (Wicker and Skamarock 2002). Advection on the first two steps uses fifth-order upwind differencing. On the final Runge–Kutta step, scalar quantities and wind components are advected with a fifth-order weighted essentially nonoscillatory (WENO) scheme (Jiang and Shu 1996; Shu 2003). Note that Mansell et al. (2010) used a sixth-order forward-in-time scheme for scalar quantities, but comparison tests found that the WENO scheme has similar accuracy along with improved consistency between hydrometeor moments (e.g., graupel mass and number concentration), which better suppresses mismatches that can cause large particles with low total mass at the edges of precipitation regions. The supersaturation is diagnosed at each time step from the predicted water vapor and temperature fields, which seem to suffer minimal cloud-edge effects because of the accuracy and adaptive filtering provided by the WENO scheme. Sedimentation uses a first-order upwind scheme, with corrections for the two-moment variables as in Mansell (2010) to prevent spurious large particles and radar reflectivity values.

b. Microphysics

The cloud model employs a two-moment bulk microphysical parameterization scheme that describes form and phase changes among a range of liquid and ice hydrometeors (Mansell et al. 2010; Ziegler 1985). The microphysical parameterization predicts the mass mixing ratio and number concentration of cloud droplets, raindrops, cloud ice crystals (columns), snow particles (including large crystals and aggregates), and graupel. The graupel particle density is also calculated by predicting the total particle volume (Mansell et al. 2010). One new enhancement to the scheme is a parameterization of the increase in particle density during melting. The previous version of the scheme kept the ice density constant during melting, which is unrealistic particularly for low-density particles. Details of the density prediction are provided in the appendix. Observations of the 29 June 2004 storm (Bruning et al. 2007) and test simulations found little evidence for large hail. The graupel category includes small hail in its size and density spectrum, whereas the hail category is designed to simulate larger hail sizes. Therefore the hail category is deactivated in this study [as in Mansell et al. (2010)] to simplify the analysis to one category of large precipitation ice. Hydrometeor size distributions are assumed to follow a gamma functional form (Mansell et al. 2010). Microphysical processes include cloud droplet and cloud ice nucleation, condensation, deposition, evaporation, sublimation, collection–coalescence, variable-density riming, shedding, ice multiplication, cloud ice aggregation, freezing and melting, and conversions between hydrometeor categories. We note that the general conclusions from the present results have been remarkably consistent through many updates to the microphysics, including tests with three-moment graupel (Mansell 2010) and prediction of liquid water on graupel (Ferrier 1994).

CCN concentration is predicted as in Mansell et al. (2010) with a bulk activation spectrum (N_{CCNa} = CCN $\times$ S^k, where $k = 0.6$) approximating small aerosols. The model tracks the number of unactivated CCN, and the local CCN concentration is depleted as droplets are activated, either at cloud base or in cloud. The CCN are subjected to advection and subgrid turbulent mixing but have no other interactions with hydrometeors; for example, scavenging by raindrops is omitted, and CCN are not restored by droplet evaporation.

c. Electrification and lightning

Electrification parameterizations follow Mansell et al. (2005, 2010), including noninductive charge transfer (i.e., independent of the ambient electric field) between graupel and smaller ice and snow particles. Inductive (i.e., field dependent) charging between graupel and small droplets is also active, as well as small ion processes (e.g., generation by cosmic rays, recombination, attachment to hydrometeors, drift, and corona point discharge at the ground). Mansell et al. (2010) found that noninductive

charging based on the work of Brooks et al. (1997) and the laboratory results of Saunders and Peck (1998) provided a good match to the observed lightning in the 29 June storm, so the same hybrid scheme is used here. All of the noninductive charge separation schemes available in the model depend on rebounding graupel–ice collisions, so generally similar modulations of charging rate magnitudes and lightning flash rates are expected for the other parameterization options [e.g., those used in Mansell et al. (2005)], although charge structure may differ substantially. In the present set of experiments, total inductive charge separation is generally an order of magnitude weaker than total noninductive charging. The laboratory study by Saunders and Brooks (1992) found that ice–ice charge separation ceased under conditions of wet growth (i.e., collecting supercooled droplet mass faster than it can all freeze) as ice crystals simply stick to the wet graupel surface. The model therefore disables collisional charge separation in wet-growth collisions, including inductive charge separation, as droplets would be expected to coalesce with the liquid surface. Lightning discharges are simulated with a stochastic 3D branched parameterization (Mansell et al. 2002) to reduce the overall electrical energy of the storm. Breakdown is initiated when the electric field magnitude exceeds a height-dependent threshold (Mansell et al. 2010), and the lightning charge is deposited as small ions. The electric potential is calculated using a parallelized version of the "black box multigrid" (BOXMG) elliptic equation solver (Dendy 1982; Moulton et al. 1998).

d. Model domain, initialization, and integration

The horizontally homogeneous model environment was initialized from the 0000 UTC 29 June 2004 National Weather Service operational sounding (Fig. 1). Sounding modifications reduced the mixed-layer convective inhibition (CIN) from 11.4 to 2.9 J kg^{-1} and increased CAPE from about 770 to 1011 J kg^{-1}. Simulations were performed in a 30 km × 30 km × 21.6 km domain with constant grid spacing of 250 m in the horizontal and 125 m in the vertical from the surface to 10 km, above which the grid spacing was gradually stretched to a maximum of 500 m. The time step was 4 s. Vertical motion was initiated by applying a constant acceleration term to vertical velocity in the boundary layer, as in Mansell et al. (2010). The updraft nudging method introduces deep moist convection more smoothly than the conventional thermal bubble initialization and is more representative of roll-type mesoscale updraft forcing of convection initiation (e.g., Ziegler et al. 1997). The same initial conditions and forcing were used for all simulations.

Two sets of simulations were run with base values of CCN concentration that varied over 13 values and two
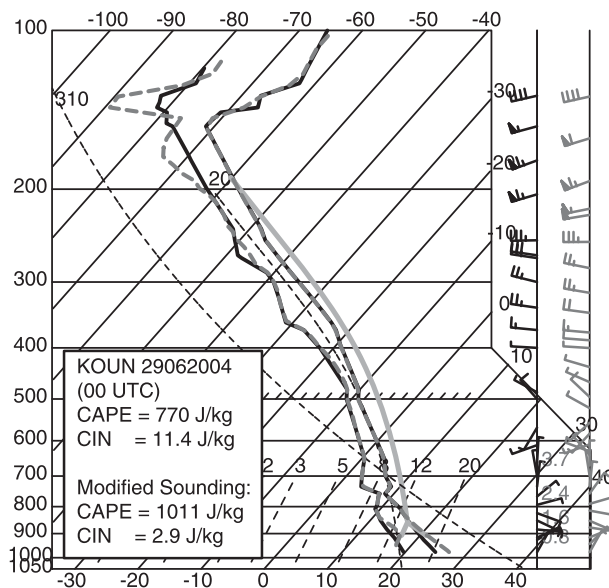

FIG. 1. Environmental sounding (solid curves) and model initialization sounding (dashed gray curves). From Mansell et al. (2010).

orders of magnitude: 50, 100, 200, 300, 500, 700, 1000, 1500, 2000, 3000, 4000, 5000, and 8000 cm^{-3}. The first set (HM1) used the Ziegler et al. (1986) parameterization of Hallett–Mossop secondary ice multiplication (Mossop 1976) that depends on the number of cloud droplets with diameter greater than 24 μm. The second set (HM2) was run with a more commonly used parameterization of Hallett and Mossop (1974) that produces 350 ice splinters per milligram of rime (e.g., Cotton et al. 1986; Ferrier 1994) and ignores (incorrectly) the droplet size spectrum. We also note that previous studies such as Cotton et al. (1986) and Beheng (1992) also included parameterizations of both forms. HM1 and HM2 both operate in the temperature range of −3° to −8°C, except when more liquid water is accreted than is able to freeze (i.e., wet-growth mode), which is assumed to preclude rime splintering as excess water is shed as raindrops. Heymsfield and Mossop (1984) found that the process is more specifically dependent on the graupel surface temperature rather than the ambient air temperature, and wet growth implies a surface temperature of 0°C, which is outside the range for splintering. The mass of ejected ice particles is assumed to be 8.57 × 10^{-12} kg for both rime splintering and raindrop freezing, corresponding to an ice column length of about 30 μm. Tests with crystal lengths of 12 μm (6.8 × 10^{-13} kg) had similar results, with about a 7%–12% reduction in electrification because of reduced charge transfer per collision for smaller crystals. As in Mansell et al. (2010), one ice splinter is produced from each freezing raindrop. Unless specified, results are shown for HM1. Initial CCN concentrations were assumed to be

vertically well mixed and therefore scaled by air density as $CCN(z) = CCN_{base}[\rho_{air}(z)/\rho_o]$. In other words, the CCN number mixing ratio (number per kilogram of dry air) was assumed to be initially uniform throughout the domain.

3. Results

a. Growth and mature stages

The simulations produce a small main storm cell with a horizontal diameter of order 3–4 km (Figs. 2 and 3). The droplet number concentrations and mass contents shown in Fig. 2 indicate that the model's warm-rain processes exhibit the expected sensitivity to increasing CCN concentration, yielding greater droplet number concentrations and cloud water contents in the towering cumulus stage. The result is consistent with two-dimensional bin models (e.g., Khain et al. 1999; Khain and Pokrovsky 2004) and previous three-dimensional bulk models (e.g., Seifert and Beheng 2006). At 35 min, the 100-cm^{-3} CCN case shows nearly complete depletion of cloud water content in the upper part of the updraft via autoconversion and collection by raindrops (Fig. 2d), whereas higher CCN cases of 500 and 5000 cm^{-3} have delayed these processes (Figs. 2e,f). Figure 2a also shows that the supersaturation (with respect to liquid water) rises significantly in updrafts where droplet scavenging is significant. Additional CCN types that activate at higher supersaturation would be able to nucleate in such regions and potentially alleviate the larger values, but Khain et al. (2012) also found similarly large supersaturations (>5%) even with such small aerosols included. Intermediate to high CCN concentrations show progressively less raindrop mass at the same times (Figs. 2e,f), allowing greater cloud water content (CWC) close to adiabatic values at higher altitudes in the updraft. The vertical gradients of CWC are very similar in rain-free regions above cloud base (i.e., where collection of droplets is not significant), indicating that the total condensation growth is comparable in those regions.

Most of the CCN are totally depleted by nucleation within the first 500–1000 m above cloud base, as inferred from the droplet concentrations (Figs. 2a–c), as was also the case in the numerical study by Fan et al. (2009), which used bin microphysics and a resolved aerosol spectrum. Compared to the spectral bin simulations of Khain et al. (1999) and the in situ observations by Konwar et al. (2012), however, the model may be nucleating too aggressively. Konwar et al. (2012) found a nonlinear relationship between CCN and droplet concentrations ($N_c \propto CCN^{0.44}$), suggesting that condensation growth of previously nucleated droplets limits the

nucleation of new drops more than is accounted for in the model. Nevertheless, the results place greater importance on the sensitivity to changes in CCN concentration (and thus droplet concentration) than on the local CCN concentration itself.

The effects of increasing CCN concentration on the warm-rain process naturally have consequences on the mature-storm morphology and on the graupel density, as shown in Fig. 3 for three CCN values at a common location and time of 53 min. Although the complex storm structures result from nonlinear evolution, Figs. 3a–c suggest larger reflectivity areas and more robust convection as CCN increases. The cloud droplet size directly affects rime density (Macklin 1962), whereby smaller droplets result in lower-density graupel (Figs. 3d–f). Graupel fall speed (actually the droplet impact speed) also modulates rime density, such that slower-falling graupel particles acquire lower density rime. The source of graupel embryos, whether frozen drops or rimed ice particles, has a further effect on the graupel density. The densification of graupel by melting is especially evident below the 0°C isotherm in Fig. 3f, where the particle densities are low before melting commences.

b. Bulk storm evolution with differing CCN

The simulated time–height reflectivity, graupel mass, rain mass, and updraft volume all show systematic variations in their evolutions as base CCN concentration increases, as illustrated in Fig. 4. At lower CCN, precipitation first initiates as raindrops via quasi-stochastic collision–coalescence in regions of high cloud water content (Figs. 4a,f). Higher CCN concentrations delay the collision–coalescence formation of drizzle-sized rain, which also shifts the initial reflectivity echoes to later times and higher altitudes (Figs. 4a–e). Raindrops lifted in updraft begin freezing at temperatures around −10°C to form graupel at low to moderate CCN concentrations (Figs. 4f–i). At higher CCN, precipitation mass gradually becomes dominated by the graupel-based, cold-cloud riming process relative to the warm-rain process (Fig. 4j).

As higher CCN concentrations cause increasing delay times for rain formation, drops appear at higher altitudes and lower temperatures (Figs. 4f–j) and have less time to collect droplets before freezing. Supercooled drizzle (small rain) appears even at the highest CCN concentrations because the vapor supply in the updraft remains sufficient for droplets to eventually grow large enough via condensation to generate some drop coalescence growth (Leighton and Rogers 1974). Increasing CCN concentration supports the general trend of delayed precipitation initiation and reflectivity echoes to later times and higher altitudes, leading also to greater graupel mass aloft (Figs. 4f–j). The time of precipitation reaching
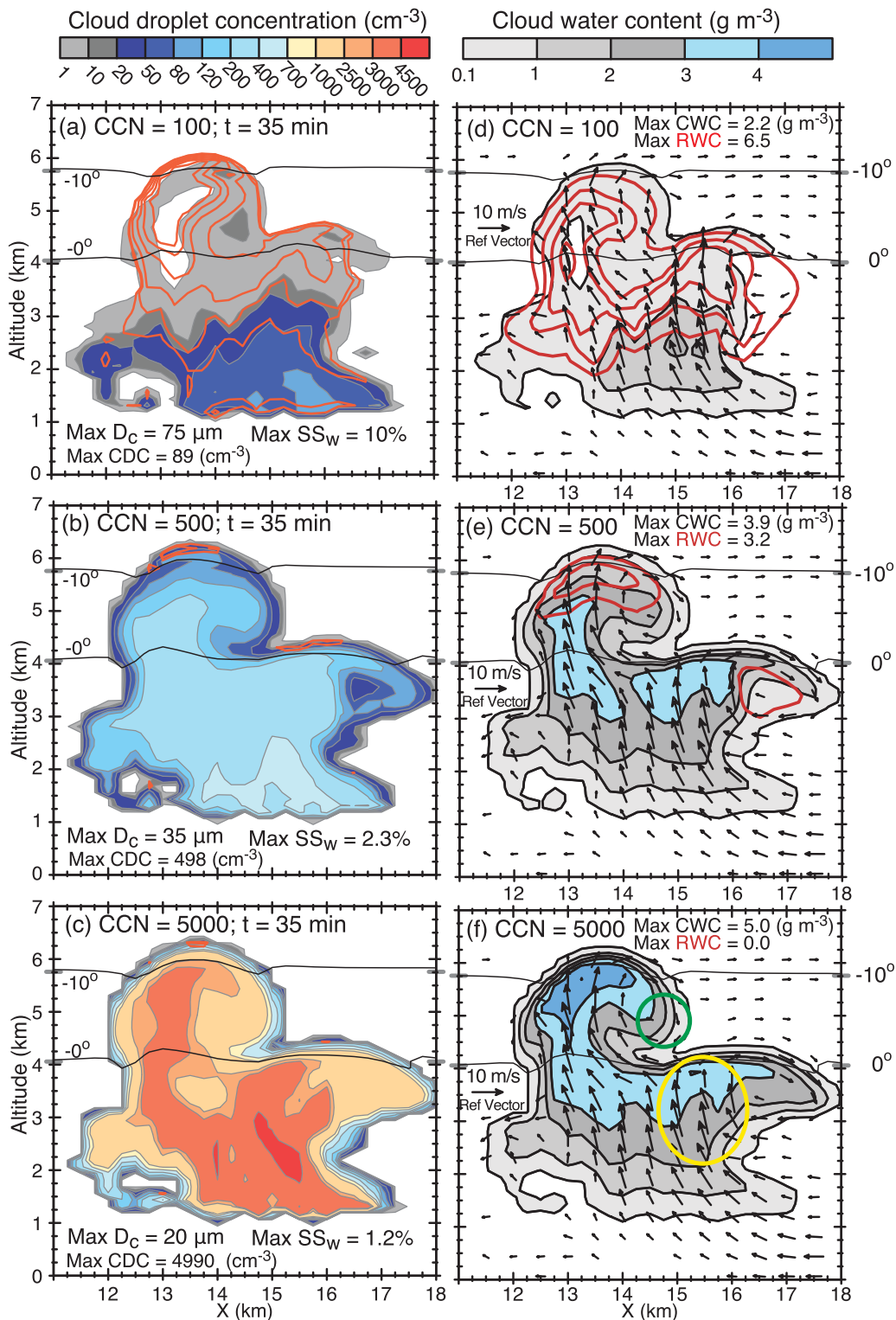
FIG. 2. (a)–(c) Droplet concentration and supersaturation (orange contours at 0.25%, 1%–9% by 2%) and (d)–(f) cloud water content (filled contours) and rain content (red contours from $1 \, \mathrm{g \, m^{-3}}$ with a $1.5 \, \mathrm{g \, m^{-3}}$ interval) in the towering cumulus growth stage (time = 35 min) for three CCN concentrations: (a),(d) 100, (b),(e) 500, and (c),(f) 5000 $\mathrm{cm^{-3}}$. The green circle and yellow ellipse in (f) denote a region of ice crystal growth and incipient deep updraft, respectively.
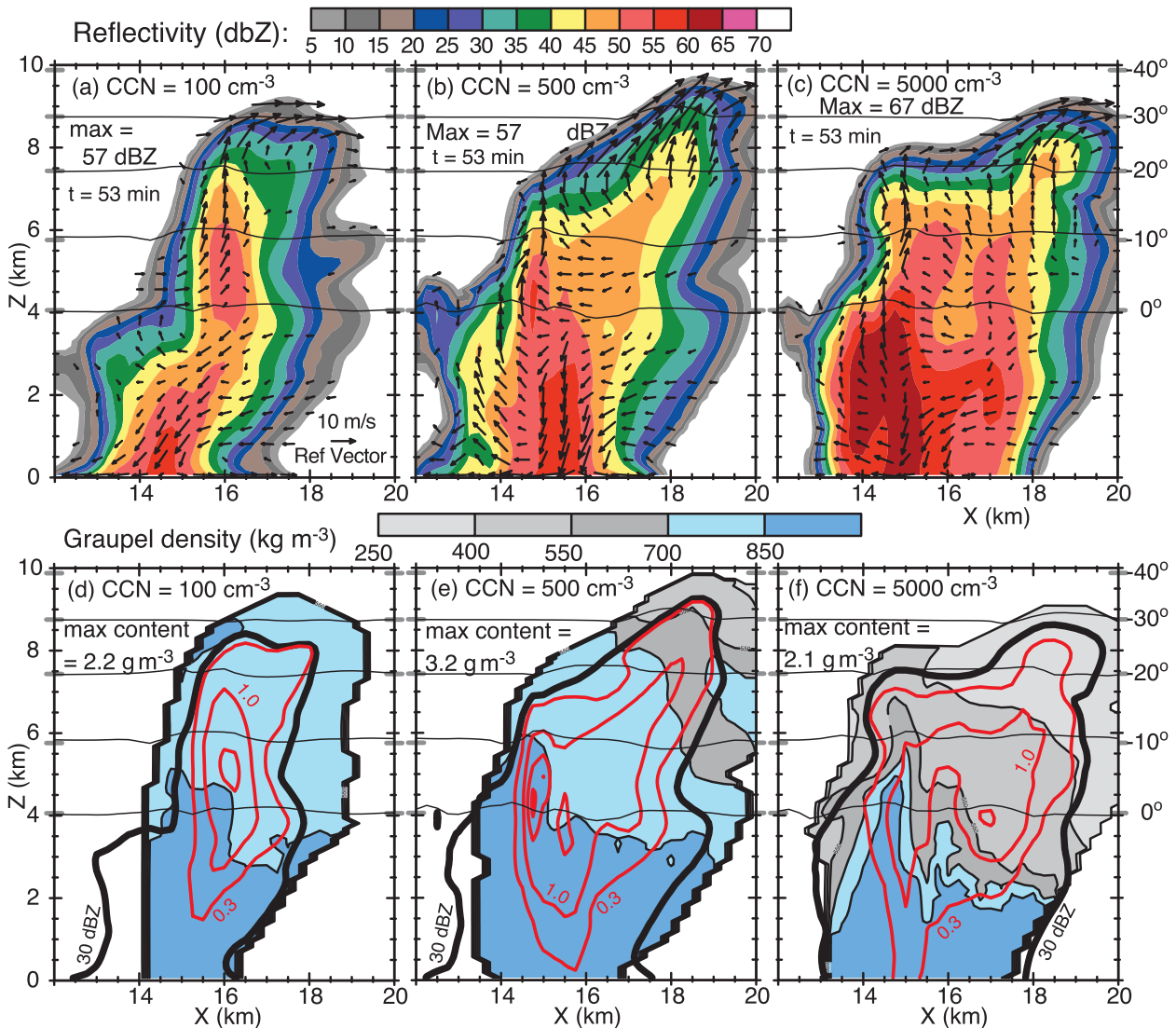
FIG. 3. (a)–(c) Simulated (Raleigh scattering) reflectivity and (d)–(f) graupel particle density (filled contours) and mass content (g m^{-3}, red contours) at 53 min for three CCN concentrations: (a),(d) 100, (b),(e) 500, and (c),(f) 5000 cm^{-3}.

the ground is also delayed by increased CCN [e.g., as in Khain et al. (2005)], with the source of initial rainfall transitioning from warm-rain-process drops to rain from melted graupel (Figs. 4f–j).

c. Electrification and lightning

The model electrification primarily comes from non-inductive graupel charging, and thus it is an expected result that lightning activity generally increases (Fig. 5) as more graupel is generated (Figs. 4f–j), but changes in ice crystal production also play an important role. Figure 5 also indicates the charge structure corresponding to lightning structure, which maintains positive charge at lower and higher altitudes (4–6 and 7–9 km), with negative charge at 5–7 km. At the lowest CCN of 50 cm^{-3},

the storm has a positive dipole structure (positive charge above negative) and a corresponding lightning structure of negatively charged channels in the positive charge region and vice versa (Fig. 5a). At CCN of 300 cm^{-3}, a lower negative dipole first develops (Fig. 5b), with an upper positive charge appearing later. Even higher CCN (1500 cm^{-3}; Fig. 5c) leads to earlier and stronger electrification, but further increases (above 2000 cm^{-3}) start to reduce the charge separation and lightning activity (Fig. 5d). Thus the charge structure tends to be a normal tripole with a relatively weak upper positive charge for most of the range of CCN. The reduction in electrification at very high CCN is not a matter of reduced graupel production, but rather how ice crystals are generated in the model as modulated by CCN, as will be discussed in the next section.
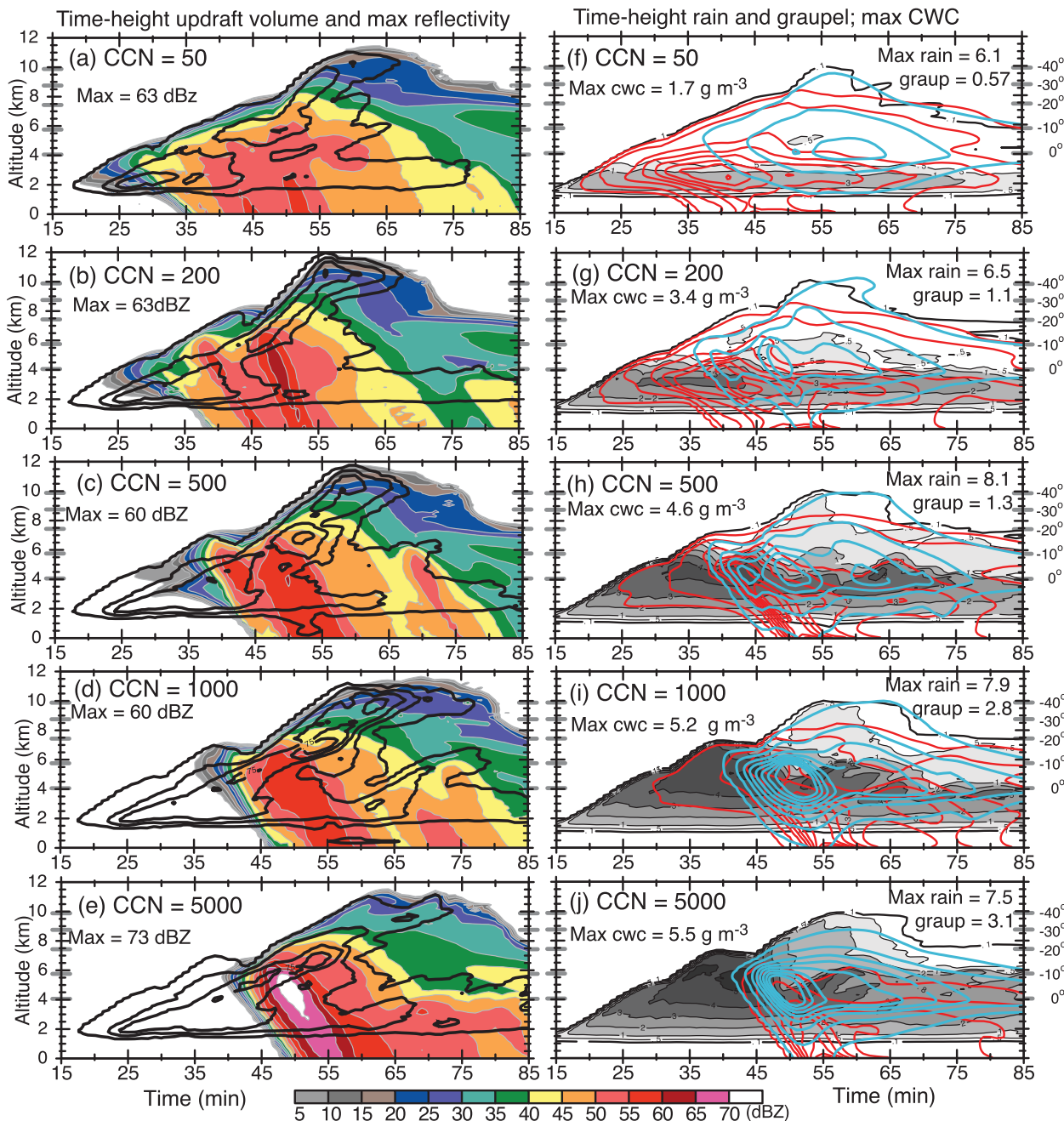
FIG. 4. (a)–(e) Time–height maximum simulated radar reflectivity (color shading) and updraft volume ($w > 5\,\mathrm{m\,s^{-1}}$; black contours at 0.01, 0.25, 0.5, 0.75, and 1 km^3 per level). (f)–(i) Time–height maximum CWC (gray shading, 0.1, 0.5, 1–5 g m^{-3}), and horizontally integrated rain (red contours) and graupel (blue contours) masses. Contour levels in (f)–(i) for graupel mass are 0.02 Tg (10^6 kg) and ≥ 0.2 Tg at an interval of 0.3 Tg, and for rain mass are 0.02, 0.2, and ≥ 0.2 Tg at an interval of 1 Tg.

4. Discussion

a. CCN effects on dynamics

The "updraft invigoration" effect (e.g., Rosenfeld et al. 2008) can be seen by the increased volume containing updraft speeds exceeding $5\,\mathrm{m\,s^{-1}}$ as CCN increases from

50 to $1000\,\mathrm{cm^{-3}}$ (time–height contours in Figs. 4a–d and time series in Fig. 6a). A secondary maximum appears at upper levels around 50–55 min (Figs. 4b–d), but weakens for CCN $\geq 5000\,\mathrm{cm^{-3}}$ (Figs. 4e and 6a). The reduction of upper-level updrafts at high CCN also inhibits the development of the upper positive charge region, with
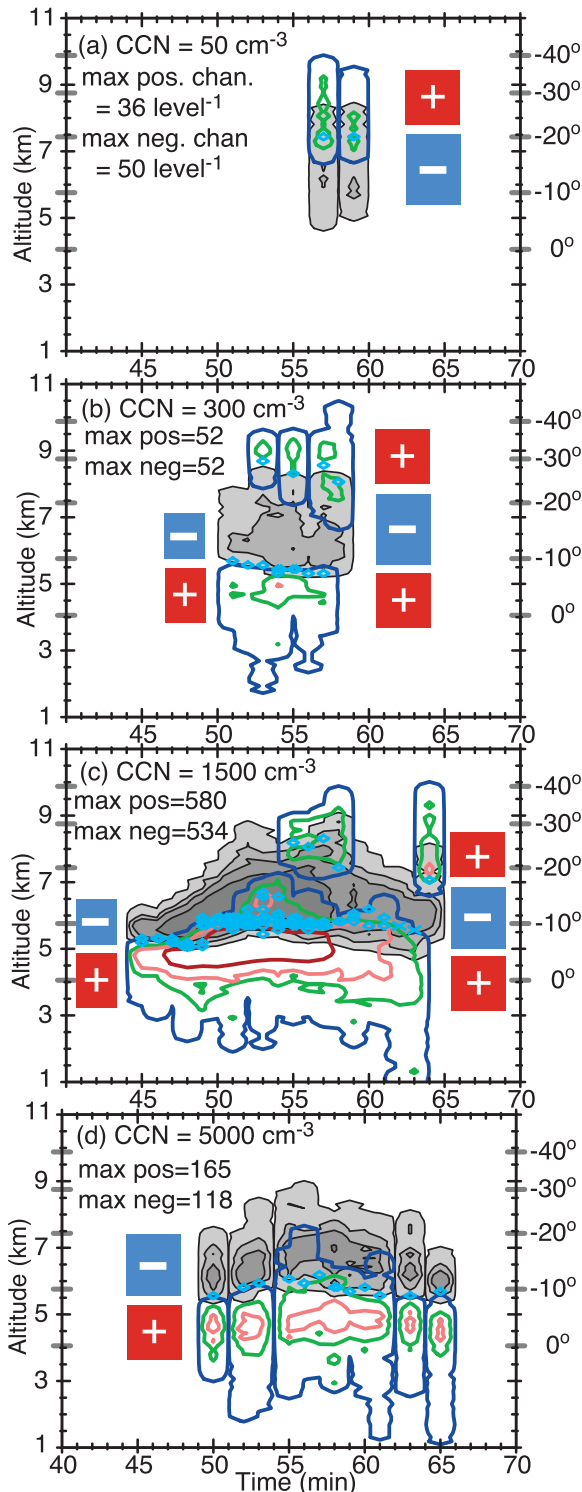
FIG. 5. Time–height lightning channel segments per model level (negatively charged: colored contours; positively charged: gray-filled contours). Contour levels are 0.75, 20, 50, and 150 segments per level. Initiation heights are indicated by diamonds (IC) and crosses (CG). The red (positive charge) and blue (negative charge) boxes indicate the vertical structure of significant charges that would be inferred from the lightning alone.

subsequent loss of lightning activity aloft (Fig. 5d). The enhancement of the updraft core is more clearly evident at a higher updraft volume threshold of $10 \, \mathrm{m \, s^{-1}}$ (Fig. 6b), reaching a maximum at a CCN concentration of $1000 \, \mathrm{cm^{-3}}$ that is maintained at higher CCN. The greater updraft core volumes are driven by increased vapor condensation to cloud droplets (Fig. 6c). The droplets are able to grow for a longer time as they start out smaller and smaller, and the delayed onset of significant autoconversion also retards loss of the droplets to scavenging, preserving a large total surface area for condensation. The limits in $10 \, \mathrm{m \, s^{-1}}$ updraft volume and condensation rate reached for CCN $\geq 1000 \, \mathrm{cm^{-3}}$ suggest that condensation latent heating has been maximized for the available vapor supply.

The weaker upper-level updrafts at very high CCN (Fig. 4e) can be attributed to a combination of increased mass loading by cloud droplets and reduced latent heating by riming freezing of cloud droplets (i.e., collection by graupel particles). Figure 7 illustrates an example of the differences between the 1000- and 5000-$\mathrm{cm^{-3}}$ CCN cases in terms of the buoyancy, calculated as

$$B = g\left(\frac{\theta'}{\overline{\theta}} + 0.61 q_v'\right) - g q_{\mathrm{tot}}, \tag{1}$$

where the first part is denoted as the thermal buoyancy (involving potential temperature θ and perturbation water vapor mixing ratio q_v') and the second part is the hydrometeor loading (with total condensate mixing ratio q_{tot}). At 49 min, total condensation is about equal for 1000- and 5000-$\mathrm{cm^{-3}}$ CCN (Fig. 6c), yet the 1000-$\mathrm{cm^{-3}}$ CCN case exhibits greater thermal buoyancy and less loading near the top of updraft (Figs. 7c,d). For 1000-$\mathrm{cm^{-3}}$ CCN, riming freezing provides additional latent heating, and subsequent sedimentation reduces parcel loading, as indicated by larger graupel mass content along with lower droplet mass content (Figs. 7f,g). Less graupel riming at 5000-$\mathrm{cm^{-3}}$ CCN, however, contributes to increased loading in the updraft parcels (e.g., Rosenfeld et al. 2008) and reduced latent heating by freezing. Point values in Table 1 emphasize the dual role played by graupel to enhance the net buoyancy via latent heating by freezing and unloading by sedimentation.

The maximum updraft speed increases from about $16 \, \mathrm{m \, s^{-1}}$ (CCN of $50 \, \mathrm{cm^{-3}}$) to almost $22 \, \mathrm{m \, s^{-1}}$ (CCN of $500 \, \mathrm{cm^{-3}}$), and levels off or slightly decreases at higher CCN (Fig. 8b). The peak values all occur very close to the times of peak $10 \, \mathrm{m \, s^{-1}}$ updraft volume (around 42–45 min; Fig. 6d). Li et al. (2008) noted a similar initial increase in peak updraft followed by minor changes at higher CCN. At extremely high CCN concentration ($>5000 \, \mathrm{cm^{-3}}$), however, Li et al. (2008) found a dramatic
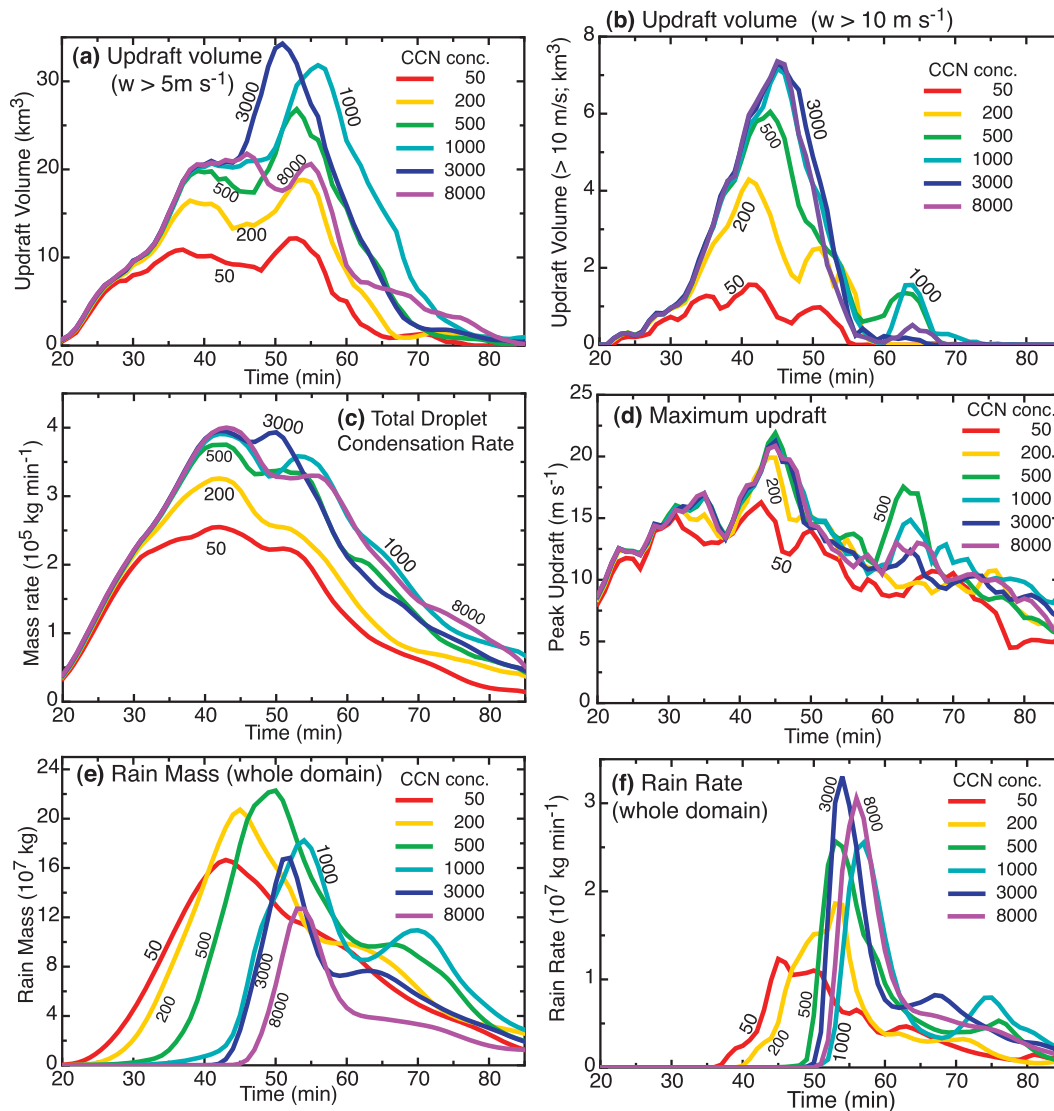
FIG. 6. Time series of volume of updraft greater than (a) 5 and (b) $10 \, \mathrm{m \, s^{-1}}$. (c) Time series of total cloud droplet condensation, (d) maximum updraft speed, (e) total rain mass, and (f) domain rainfall rate.

reduction in maximum updraft that they attributed to reduced freezing. The present results show no substantial decrease in peak updraft, even for an extra simulation with CCN of $15\,000 \, \mathrm{cm^{-3}}$ (not shown). Differences in grid resolution, storm initialization, and storm evolution might explain the discrepancy, particularly if the peak updraft in Li et al. (2008) was reached at upper levels of the storm, where indeed a reduction in updraft volume ($w > 5 \, \mathrm{m \, s^{-1}}$) at upper levels is noted in the present results.

The effects of varying downdraft intensity can be discerned in the time–height contours of $5 \, \mathrm{m \, s^{-1}}$ updraft volume (Figs. 4c,d) below 1.5-km altitude. As a cold downdraft impinges on the surface, the air spreads out along the ground as a density current and lifts the warmer ambient air as it propagates. The low-level lifting from cold air outflow is weaker for CCN $\leq 200 \, \mathrm{cm^{-3}}$, then stronger for 500–1000-$\mathrm{cm^{-3}}$ CCN concentration (at around 46 and 55 min for 500 and $1000 \, \mathrm{cm^{-3}}$, respectively; Figs. 4c,d). The low-level lifting is reduced again for CCN of $5000 \, \mathrm{cm^{-3}}$ (Fig. 4e). The negative buoyancy of the downdraft air results from a combination of the hydrometeor loading and cumulative cooling by melting of ice and evaporation of rain. Loading and cooling increase as the precipitation rates become more intense (Fig. 6f), but at very high CCN evaporation decreases while the peak rain rates remain somewhat constant. The decreased evaporation arises from a transition
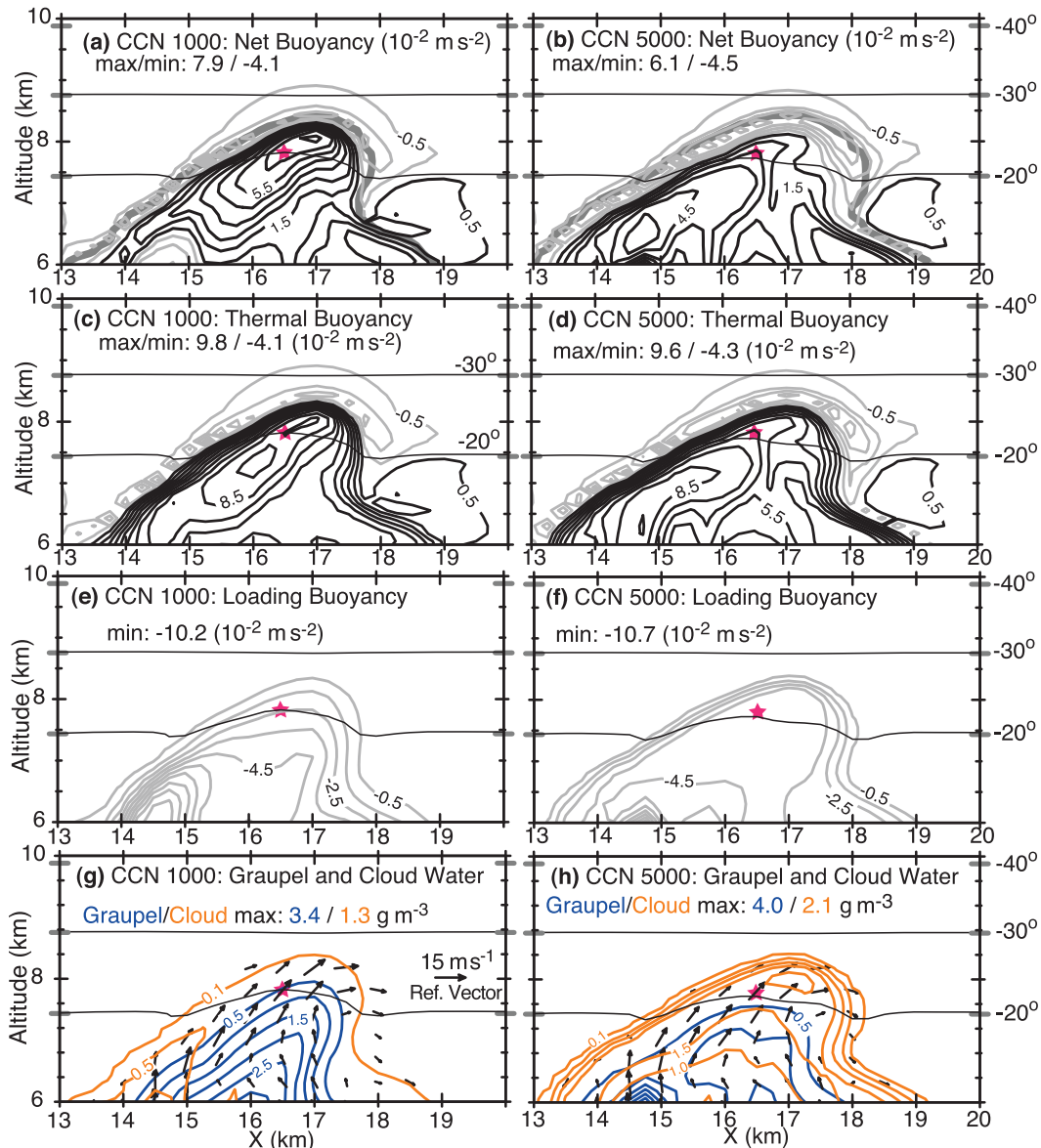
FIG. 7. Buoyancy differences for CCN of (left) 1000 and (right) 5000 cm^{-3}. (a),(b) Net buoyancy, (c),(d) thermal buoyancy, and (e),(f) mass loading have black contours for positive values and gray for negative, intervals of 1. (g),(h) Graupel (blue) and cloud droplet (orange) mass content, contour levels of 0.1 g m^{-3} and from 0.5 g m^{-3} by 0.5 g m^{-3}. Values at the star shown are given in Table 1.

to larger raindrops (from larger melted graupel), which evaporate more slowly than small drops.

b. Transition in dominant precipitation type

The initial transition from low to medium CCN (from 50 to 500 cm^{-3}) has an increase in maximum rain mass (per model level) from 6.1 to 8.1 Tg (Figs. 4f–h), with peak domain-integrated masses occurring at successively later times (Fig. 6e). This rise in maximum rain mass results from a marked increase in total cloud droplet quasi-stochastic collection by rain (powered by

greater latent heating and updrafts), although the total number of drops produced by autoconversion remains fairly constant (Fig. 8a). Collection is always a much greater source to rain mass than the initial source of autoconverted droplets (Fig. 8a), as previously noted by Wang (2005). As CCN concentration exceeds 500 cm^{-3}, autoconversion and collection both decline monotonically (Fig. 8a), implying that the warm-rain process is responsible for maximizing the total rain mass (Fig. 6e) at around 500 cm^{-3}. Higher CCN (>500 cm^{-3}) reduces the maximum domain-integrated rain mass, particularly at

TABLE 1. Quantities at the point indicated in Fig. 7.

Quantity	CCN = 1000 cm^{-3}	CCN = 5000 cm^{-3}
Buoyancy: Net (m s^{-2})	7.1×10^{-2}	2.8×10^{-2}
Buoyancy: Thermal (m s^{-2})	9.6×10^{-2}	6.8×10^{-2}
Buoyancy: Load (m s^{-2})	-2.5×10^{-2}	-4.0×10^{-2}
Cloud mass (g m^{-3})	0.37	1.9
Graupel mass (g m^{-3})	0.57	0.21
Total mass (g m^{-3})	1.3	2.1
Perturbation virtual potential temperature θ_v' (K)	3.2	2.3
Vertical velocity (m s^{-1})	9.9	9.3
SS$_w$ (%)	1.4	0.04
Droplet concentration (cm^{-3})	58	1050
Mean droplet diameter $\overline{D}_c$ (μm)	23	15

subfreezing temperatures, as warm-rain production decreases and graupel initiation and mass increase. Graupel melting then becomes responsible for the peaks in rain mass at later times for higher CCN (Fig. 6e).

The transition from drop freezing to snow riming as the primary source of graupel embryos occurs over the CCN range of 700–5000 cm^{-3}. The number of initiated graupel particles increases steeply (Fig. 8c) from 500 to 1000 cm^{-3} as drop freezing peaks and riming conversion of snow to graupel becomes more significant. Then drop freezing falls off as raindrop initiation (i.e., autoconversion)

decreases. Graupel initiations (Fig. 8c) and time-integrated mass (Fig. 9a) both maximize at CCN of about 2000 cm^{-3}, where initiations by drop freezing and snow riming make equal contributions (Fig. 8c). The trends in time-integrated graupel mass (Fig. 9a) directly follow those in the graupel initiations with maxima at CCN of 2000 cm^{-3}.

c. Rainfall and rain rate

The total rainfall (Fig. 8b) follows the trend of increasing rain accretion at lower CCN (50–500 cm^{-3}), with further increase at high CCN (1000–5000 cm^{-3}) as graupel
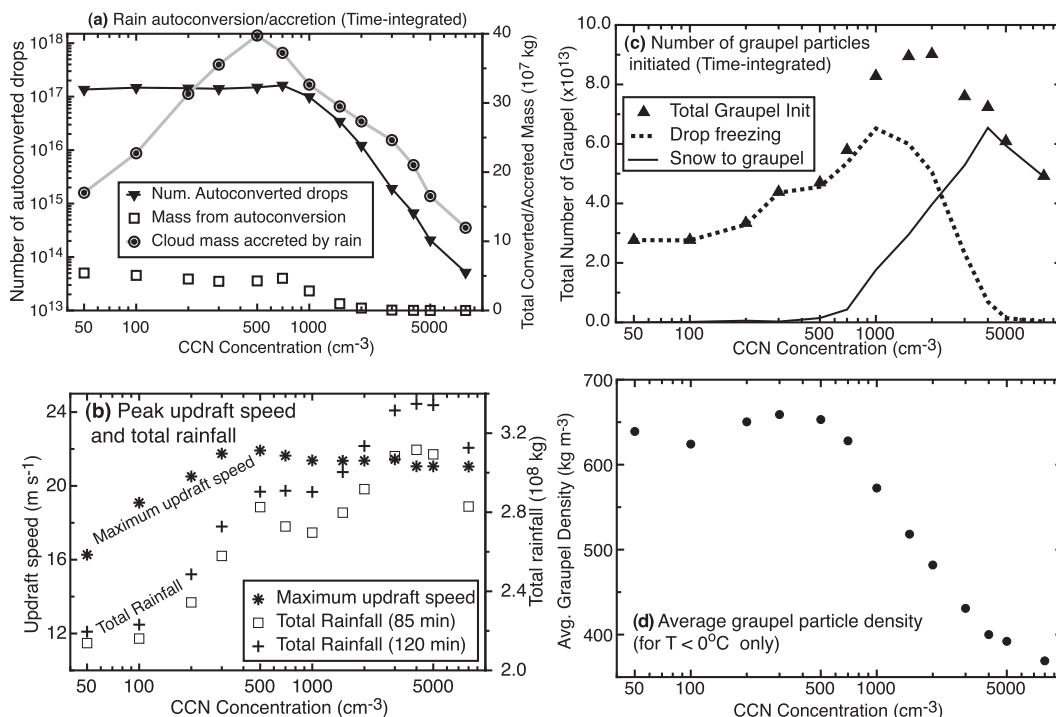

FIG. 8. Aspects of precipitation for varying CCN concentration. (a) Time-integrated total raindrop production by autoconversion and droplet accretion by rain. (b) Maximum updraft speed and total rainfall. (c) Time-integrated total graupel production by "warm" (drop freezing) and "cold" (snow riming) processes. (d) Time- and domain-averaged graupel particle density.
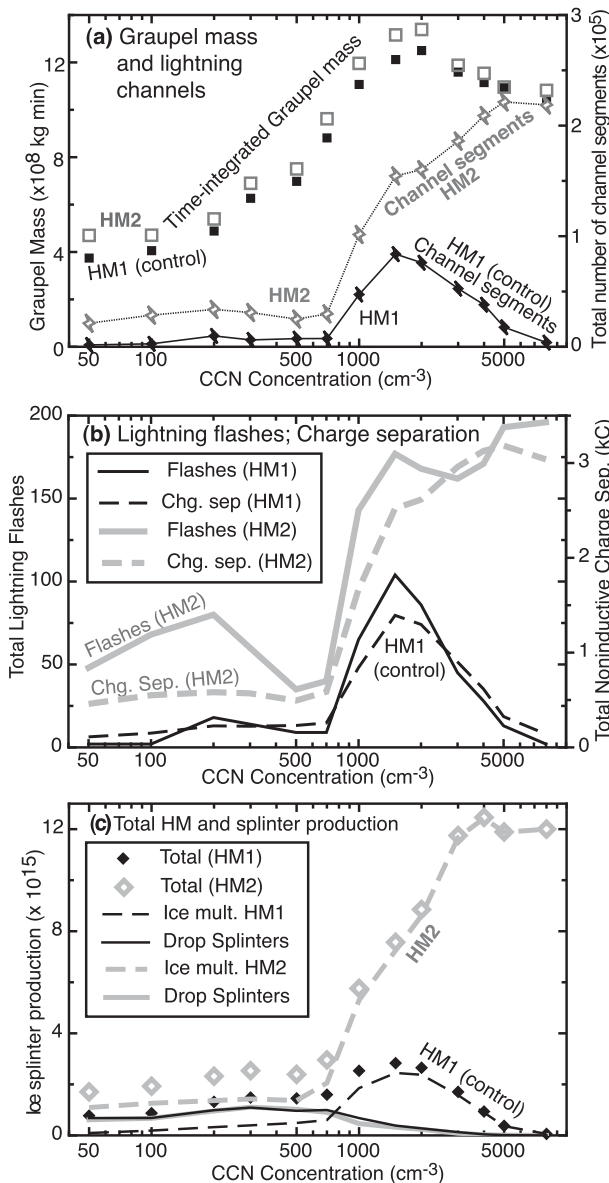
FIG. 9. Graupel mass, ice crystal production, and lightning sensitivity for varying CCN concentration. (a) Time-integrated total lightning flashes and noninductive charge separation for HM1 (sensitive to droplet size; black) and alternate HM2 (rime mass only; gray) Hallett–Mossop ice-multiplication parameterizations. (b) Time-integrated graupel mass and lightning channel segments for HM1 and HM2. (c) Time-integrated ice crystal production by ice multiplication (HM1, HM2) and splinters from freezing drops.

production grows. The same basic trend is seen both for the original 85-min simulations and for extensions to 120 min, which were run to allow more time for storm dissipation (e.g., for sedimentation of the lingering rain and graupel masses at 85 min in Figs. 4f–j). The total rainfall starts to decline at the very highest CCN ($8000\,cm^{-3}$), which continues for an additional simulation

with CCN of $15\,000\,cm^{-3}$ (not shown). The downturn seems to be due to reduced scavenging of supercooled cloud droplets, reflected in lower time-integrated graupel mass and higher cloud water content at subfreezing temperatures (Fig. 4j, particularly above the 0°C isotherm after 50 min). The reduced total riming could arise from a combination of fewer graupel particles (Fig. 8c) along with lower graupel–droplet collection efficiency for very small droplets.

Li et al. (2008) found a similar pattern of gradually increasing precipitation, but with a much steeper decline at very high CCN. Storer et al. (2010), on the other hand, noted monotonically decreasing total precipitation for increasing aerosol concentration. Both studies used two-moment bulk microphysics and a wide range of CCN, but very different environments. The sounding used in Li et al. (2008) is more similar to the present results (relatively weak shear and weaker lapse rates above 400–500 hPa) whereas Storer et al. (2010) studied a stronger storm in a high-shear, deeper-CAPE environment. Khain et al. (2005) noted that precipitation could increase or decrease with aerosols, depending on the type of convection (deep or shallow), the humidity profile, and other factors. Fan et al. (2009) also found monotonically decreasing total precipitation with higher CCN in strong wind shear environments, but more variable total precipitation for weak wind shear.

Lynn et al. (2005) noted an increase in rainfall rates with higher aerosol content for a squall line simulated with bin microphysics, and the present results also suggest an intensification of rainfall rates (Fig. 6f). Larger maximum layer rain mass values below the melting level for higher CCN ($\geq1000\,cm^{-3}$) can be noted in Figs. 4i,j, although the peak domain rain masses decline (Fig. 6e). This suggests that the transition to a cold-rain process also tends to intensify precipitation rates and creates a more abrupt onset of high rain rates.

d. Graupel density

The average graupel density drops monotonically for CCN $> 500\,cm^{-3}$ (Fig. 8d) as a result of decreasing average embryo density as well as reduced rime density. Rime density itself decreases with declining graupel fall speed and smaller droplet size. This does not mean that all graupel is low density, however, as the average is influenced by slower-falling graupel with longer residence time. The formation of larger, high-density graupel (like small hail) actually is more evident at high CCN and causes the much larger simulated radar reflectivity values (>70 dBZ) that appear in the high range (3000–$8000\,cm^{-3}$) of CCN concentration (Fig. 4e). (We note that the simulated reflectivity values likely have a high bias resulting from the inverse exponential size distribution—i.e.,

an assumed shape parameter value of zero.) In the 5000-cm^{-3} CCN case, graupel particles first form near the edge of the initial cloud turret. The green circle in Fig. 2f denotes the region where ice crystals growing by vapor deposition begin to convert to larger snow crystals. When the snow crystals acquire rime deposits with densities greater than $200\,\mathrm{kg\,m^{-3}}$, low-density (200–$300\,\mathrm{kg\,m^{-3}}$) graupel is produced. These initial seed graupel are then entrained into a new updraft pulse (yellow ellipse in Fig. 2f), where they encounter high ambient cloud droplet mixing ratios and grow rapidly. As the graupel sizes and fall speeds increase, wet growth quickly ensues at a relatively high ambient temperature (around $-8°$C). The graupel densifies via soaking of slower-freezing liquid and sheds excess liquid as large ($>1\,\mathrm{mm}$) raindrops, leading to a region with a large mass of high-density particles (i.e., graupel mean-volume diameters of $6\,\mathrm{mm}$ and larger) representing pea-sized hail, with some larger particles (unrealistically) in the tail of the inverse exponential distribution.

e. Electrification dependence on graupel and ice crystal production

Since the charge separation parameterization depends on graupel–ice collisions in mixed-phase updrafts, the significant effects of CCN concentration on storm microphysical structure directly affect electrification and lightning activity. Lightning flash rates are known to be correlated with updraft volume and precipitation ice mass (e.g., Petersen et al. 2005; Wiens et al. 2005; Deierling and Petersen 2008), although with wide variability, particularly for lower-flash-rate storms. The changes in graupel mass for the HM1 simulations (Fig. 9a, black symbols) seem to correspond fairly well with the total lightning channel segments, particularly the maxima near CCN of 1500–$2000\,\mathrm{cm^{-3}}$. Total lightning segments closely corresponds to total channel length, which is insensitive to whether flashes are small and frequent or larger and fewer in number, and therefore is used here as a more consistent measure of lightning activity than the total number of flashes (Fig. 9b), which has greater variability. For example, total flashes for HM2 has a notable minimum at CCN of 500–$700\,\mathrm{cm^{-3}}$, but the total segments and charge separation show only slight changes. Although both graupel mass and total lightning channels decrease as CCN concentration increases from 2000 to $8000\,\mathrm{cm^{-3}}$, the decline in lightning is much greater than would be expected from the mild drop in graupel mass. On the other hand, the total charge separation (Fig. 9b; HM1) closely mirrors the total lightning segments, indicating that although graupel mass is still copious, the graupel somehow becomes less effective at charge separation at very high CCN.

Aside from graupel mass, two factors in the graupel field that affect electrification are the number concentration and particle density (Figs. 8c,d). The collision rate depends on the ice crystal concentration and the graupel sweep-out volume, $\overline{V}_{T,g}A_g$ (fall speed multiplied by the total area projection). The total projected area A_g is proportional to the mean diameter $\overline{D}_g$ and number concentration as $A_g \propto N_g\overline{D}_g^2$, and the fall speed depends on graupel diameter, particle density ρ_g, and drag coefficient C_D as $\overline{V}_{T,g} \propto (\rho_g\overline{D}_g/C_D)^{1/2}$. The mean diameter itself is a function of the mass mixing ratio q_g, number concentration N_g, and particle density as $\overline{D}_g \propto [q_g/(N_g\rho_g)]^{1/3}$. The sweep-out volume therefore is proportional to $N_g^{1/6}q_g^{5/6}C_D^{-1/2}\rho_g^{-1/3}$, so some weak reduction in electrification would be expected as N_g declines (for constant or declining q_g) and is nearly linear in mixing ratio q_g. The drag coefficient is parameterized to decrease linearly as particle density increases, so the lower particle densities at high CCN (Fig. 8d) also lead to slightly lower sweep-out volume via lower fall speed. The changes in graupel mass and number, however, cannot account for the dramatic drop in noninductive charge separation and lightning flashes (Fig. 9b) for the HM1 simulations at high CCN, since copious graupel mass is still produced.

The other requirement for electrification—smaller ice crystals—holds the answer to the lightning decrease: ice crystal production, specifically via the Hallett–Mossop (HM) process, peaks at CCN of about $1500\,\mathrm{cm^{-3}}$ (Fig. 9c; HM1), coincident with the peaks in charge separation and lightning. HM1 ice multiplication then drops rapidly at higher CCN, cutting off the supply of crystals for noninductive charge separation. Ice crystal production at lower CCN ($<700\,\mathrm{cm^{-3}}$) is fairly constant for both ice multiplication and splintering from freezing drops. Ice multiplication rapidly exceeds drop splintering at higher CCN ($>700\,\mathrm{cm^{-3}}$) as graupel production and riming increase, while reduced warm-rain processes result in fewer freezing drops.

Why does ice multiplication drop dramatically at very high CCN while total riming growth does not decrease very much? The HM1 parameterization's dependence on the number of droplets with diameters greater than $24\,\mu\mathrm{m}$ explains the reduction in ice multiplication at high CCN: the droplet sizes become too small for the rime splintering mechanism to be effective, since the tail of the size distribution has fewer larger droplets. The present findings are consistent with Takahashi (1984), who compared maritime (low CCN) and continental (high CCN) simulations of a wintertime thunderstorm and noted, "Ice multiplication does not work in the continental case because of small cloud droplets." The Takahashi (1984) spectral bin microphysics (Takahashi

1976) also parameterized ice multiplication on the capture of large droplets (Mossop 1976), and the environment had relatively low water vapor, such that moderate CCN was sufficient for reducing droplet diameters below $24 \mu m$.

To further test the sensitivity to ice multiplication, a second set of simulations was run with an alternate parameterization (HM2) based on Hallett and Mossop (1974) that incorrectly ignores droplet size and depends only on rime accretion. HM2 produces more ice crystals than HM1 at all CCN values (Fig. 9c), and it follows the same pattern of shallow increase at low CCN with larger increase through $700–1500 \, cm^{-3}$. Above CCN of $1500 \, cm^{-3}$, however, HM2 continues to increase until reaching a plateau above $3000 \, cm^{-3}$, which is in stark contrast to HM1. The high CCN plateau indicates that total dry-growth riming maintains high values in the Hallett–Mossop temperature range ($-3°$ to $-8°C$). Charge separation (Fig. 9b; HM2) and total channel segments correspond very well to the ice crystal production, maintaining strong electrification at even the highest CCN. The time-integrated graupel masses for HM2 are consistent with HM1 (Fig. 9a), though slightly higher owing to an increase in number concentration from enhanced drop freezing via ice crystal capture. Other aspects of charge structure, such as the weakening of the upper positive charge region at very high CCN, are consistent in the HM2 simulations (not shown).

One further simulation was run with CCN of $1500 \, cm^{-3}$ and all ice multiplication excluded, with the result that no lightning occurred at all (not shown). Some electrification did occur (up to $60 \, kV \, m^{-1}$ electric-field magnitudes) since ice crystals are still produced by drop freezing splintering and vapor nucleation. Simulations of deeper, higher-instability convection produce more vapor-nucleated ice crystals (not shown) at lower temperatures ($T < -20°C$) and thus are still able to produce lightning with the Hallett–Mossop rime-splintering mechanism deactivated.

5. Summary and conclusions

The general results support the conclusion that the present bulk microphysical model responds to changes in CCN in physically realistic ways in the microphysics, kinematics, and electrification. Consistent sensitivities, for example in peak updraft and total precipitation, were noted from Li et al. (2008) for a rather similar environment, despite independent microphysical models and much different spatial resolution. The present model results highlight sensitivity in graupel initiation, graupel particle density, and electrification and lightning. Charge separation and lightning increased weakly with increasing

CCN at lower values ($<1000 \, cm^{-3}$) but more dramatically with greater ice multiplication (Hallett–Mossop process) in the range of $1000–2000 \, cm^{-3}$. For concentrations of CCN $> 2000 \, cm^{-3}$, lightning decreased again for the HM1 parameterization as the number of larger cloud droplets decreased. When droplet sizes are ignored in the ice-multiplication process (the HM2 parameterization), lightning continued to increase and maintain high flash rates even at extremely large CCN concentration.

While the general microphysical contrast between low and high CCN contents is fairly well understood (e.g., Khain et al. 2005), the examination of a wide range of CCN concentration brings focus on the details of the transition. In particular, the first transition from low to medium CCN concentration delays the warm-rain process, but at the same time can enhance total warm-rain production via increased condensation leading to up-draft invigoration and maximization of cloud droplet collection by rain. A similar increase in collection was found by Wang (2005), but a subsequent decrease at higher CCN was not noted, perhaps because of the tropical environment (very deep warm-cloud depth) and the squall-line mode of convection in that study. The present case was isolated convection with a somewhat deep ($>2 \, km$) warm-cloud depth and relatively high humidity, likely making the CCN effects more apparent (e.g., Fan et al. 2007).

The present results lend support for the aerosol hypothesis for electrification and that it likely plays a role in the maritime–continental lightning contrast. The simulations are consistent with observational inferences that aerosols may enhance lightning production when meteorological conditions are similar (e.g., Yuan et al. 2011). Aerosols have multiple influences, however, such as on updrafts and ice crystal production via ice multiplication, and the simulated relationship between lightning and aerosols is not necessarily monotonic. Depending on the environment, sufficiently high CCN may shut down precipitation altogether (e.g., Li et al. 2008) or affect charge separation by modulating secondary ice multiplication. For example, environments with less boundary layer moisture (i.e., larger surface dewpoint depression) would have higher cloud bases, and added CCN could more easily suppress droplet size in the ice-multiplication zone ($-3°$ to $-8°C$). This may be a factor in delaying the generation of lower charge regions and the onset of cloud-to-ground lightning, as often occurs in storms on the U.S. high plains (MacGorman et al. 2011).

The simulations do not suggest a strong effect on storm charge structure polarity, particularly whether cloud-to-ground lightning lowers primarily positive or negative charge to the ground. One consideration is that

TABLE A1. Processes affecting graupel mass and volume mixing ratios. A density of ρ_g indicates that the current graupel density is used (i.e., does not affect the density). For this study, the minimum and maximum graupel densities ($\rho_{g,\min}$ and $\rho_{g,\max}$) were 170 and 900 kg m^{-3}.

Processes $\Delta q_{\mathrm{proc}}/\Delta\tilde{v}_{\mathrm{proc}}$	Description	Conversion density (kg m^{-3})
qracig/vracig	Drop freezing by ice capture	900
qfrzg/vfrzg	Drop freezing by Bigg process	900
qgacw/vgacw	Accretion of cloud droplets	Eq. (A2)
qgacr/vgacr	Accretion of supercooled raindrops	900
qgacs/vgacs	Accretion of snow	$\rho_{g,\min}$
qgaci/vgaci	Accretion of ice crystals	$\rho_{g,\min}$
qgdpv/vgdpv	Vapor deposition	$\rho_{g,\min}$
qgcns/vgcns	Conversion of snow to graupel	Eq. (A3)
qgcni/vgcni	Conversion of ice crystals to graupel	Eq. (A3)
qgmlr/vgmlr	Melting of graupel to rain	ρ_g
qgsbv/vgsbv	Sublimation	ρ_g
qgshdr/vgshdr	Shedding during wet growth	(NA, see text)
–/vgsoak$_{\mathrm{wet}}$	Soaking during wet growth	(NA, see text)
–/vgsoak$_{\mathrm{mlt}}$	Soaking during melting	(NA, see text)
qhcng/vhcng	Conversion of graupel to hail	ρ_g
qgwet/vgwet	Portion of liquid that freezes under wet growth	900

the current parameterizations of noninductive graupel–ice charging in the model do not take droplet size into account. The laboratory studies by Avila et al. (1998) and Avila and Pereyra (2000) found that large droplets in the size spectrum caused graupel to charge more negatively. That outcome was contrary, however, to results from Takahashi (1978), who found that charge separation was insensitive to droplet size, leaving open the question of how droplet size might affect storm charge structure, whether by increased aerosols (e.g., Lyons et al. 1998) or decreased water vapor (e.g., Carey and Buffalo 2007). In a numerical study, Mitzeva et al. (2005) considered the effects on charge separation between graupel and ice crystals of vapor released by droplets as they freeze on the graupel surface, but laboratory data do not yet exist to compare their results. If droplet size affects its freezing rate or otherwise influences the local water vapor field at the graupel surface, one could speculate that aerosols could then affect the polarity of charge separation by this means, as well.

APPENDIX

Graupel Volume Parameterization Details

Mansell et al. (2010) included a prediction of particle volume content $\tilde{v}$ to track average particle density as $\rho_g = \rho_{\mathrm{air}} q_g / \tilde{v}$, with a corresponding variable terminal fall speed, but lacked some details which are presented here. The actual advected variable is the integrated particle volume mixing ratio $v^* = \tilde{v}/\rho_{\mathrm{air}}$, which is converted to $\tilde{v}$ within the microphysics. Farley (1987) first implemented variable-density hail in a spectral bin scheme. Connolly et al. (2006) also implemented variable-density graupel in a bulk scheme, but used a fall speed formulation that was independent of particle density, which Milbrandt and Morrison (2013) showed severely limits the benefits of predicting density. Milbrandt and Morrison (2013) take a somewhat different approach to volume prediction, so some greater detail is provided here to augment and update the general approach described in Mansell et al. (2010), a version of which is included in the Weather Research and Forcasting (WRF) model as of version 3.4.

Each process (denoted generically by subscript "proc") that changes graupel mass or phase has a corresponding rate of volume change. Generally, the volume rates $\Delta\tilde{v}_{\mathrm{proc}}$ are derived from the mass mixing ratio rates Δq_{proc} using an appropriate conversion density ρ_{conv}:

$$\Delta\tilde{v}_{\mathrm{proc}} = \rho_{\mathrm{air}}\Delta q_{\mathrm{proc}}/\rho_{\mathrm{conv}}, \tag{A1}$$

where ρ_{air} is the local air density. Table A1 lists the relevant processes and ρ_{conv} values for graupel. The final total mass and volume then determine the final particle

density. The final volume change is the sum of all the "v" terms in Table A1. The Δq_{proc} rates are described in Mansell et al. (2010) and not repeated here.

For graupel accreting cloud droplets in dry-growth mode, the average rime density follows Rasmussen and Heymsfield (1985):

$$\rho_{g,rime} = c_{r1} \left[\frac{0.5 \times 10^6 D_w (0.6 \overline{V}_{T,g,m})}{-(T - T_0)} \right]^{c_{r2}}, \quad (A2)$$

where D_w is the mean volume droplet diameter, $\overline{V}_{T,g,m}$ is the mass-weighted graupel fall speed, and T is the graupel surface temperature (assumed to be equal to the air temperature). [The equation in Mansell et al. (2010) subtracted the droplet fall speed V_w, but the actual code neglects it.] The constant values are $T_0 = 273.15$ K, $c_{r1} = 300$, and $c_{r2} = 0.44$. Similar forms of variable rime-layer density have been employed previously in Lagrangian hail growth models (e.g., Ziegler et al. 1983; Xu 1983).

When graupel collects supercooled raindrops, the resulting rime is assumed to have a density of 900 kg m^{-3}, though this may overestimate the density for very small, drizzle-sized drops. In wet-growth mode, the frozen portion of collected supercooled water (cloud droplets and/or raindrops) is allowed to soak into the ice matrix and increase the bulk density if it is currently less than 900 kg m^{-3} (described below). Collected ice crystals and snow and vapor deposition are assumed to add volume at the minimum density allowed for graupel (170 kg m^{-3}).

The density of graupel embryos generated by riming of ice crystals or snow is determined from the average of the crystal or snow density and the instantaneous rime density. The rime density comes from Eq. (A2) by substituting the crystal (or snow) fall speed for the graupel fall speed:

$$\rho_{conv,x} = (\rho_{x,rime} + \rho_x)/2, \quad (A3)$$

where x represents ice crystals or snow particles. A threshold rime density of 200 kg m^{-3} is required for conversion to ensure that riming is sufficient to become graupel. The resulting $\rho_{conv,x}$ is limited to the range of allowed graupel densities, which in the current study is 170–900 kg m^{-3}.

Wet growth occurs when graupel collects cloud droplets and raindrops at a faster rate than can freeze via heat balance, and the excess water is shed as raindrops. The rime density is assumed to be a maximum (900 kg m^{-3}) during wet growth. If the current graupel density is less than the maximum (i.e., $\rho_g < \rho_{g,max}$), then the accreted mass is allowed to fill in air gaps in the porous rime. The interstitial volume that is available for filling $\tilde{v}_{avail}$ is the difference between the total particle volume and the volume that the same mass would occupy at the $\rho_{g,max}$:

$$\tilde{v}_{avail} = (1 - \rho_g/\rho_{g,max})\tilde{v}_g, \quad (A4)$$

and the volume rate of new mass vgwet is

$$vgwet = \rho_{air} qgwet/\rho_{g,max}, \quad (A5)$$

where qgwet is the mass freezing rate. The volumetric soaking rate is then

$$vgsoak_{wet} = -\min(\tilde{v}_{avail}/\Delta t, vgwet), \quad (A6)$$

where Δt is the time step. A similar soaking rate formulation was also used in the hail growth model of Ziegler et al. (1983).

The rate of volume lost to shedding during wet growth is the difference between the retained and accreted volumes:

$$vgshdr = vgwet - vgacw - vgacr. \quad (A7)$$

Note that vgacw and vgacr are calculated under and initial assumption that all of the liquid freezes (i.e., dry growth), so vgshdr represents the portion that did not actually freeze because of heat balance.

A new feature added to the scheme for the present simulations is a volume change during melting of graupel that simulates the soaking of meltwater into the ice matrix. The procedure follows the wet-growth soaking, but the available volume is first adjusted by the amount already melted during the time step:

$$\tilde{v}_{avail:mlt} = (1 - \rho_g/\rho_{g,max})(\tilde{v}_g + vgmlr\Delta t), \quad (A8)$$

where vgmlr ≤ 0. The full volume of the melted mass (vgmlr = ρ_{air}qgmlr/ρ_g, where qgmlr ≤ 0) is assumed to be available to fill the air voids, such that the rate of volume lost to soaking (i.e., particle collapse) is

$$vgsoak_{mlt} = -\min(\tilde{v}_{avail:mlt}/\Delta t, |vgmlr|). \quad (A9)$$

The result allows low-density graupel to realistically collapse to a higher-density particle with correspondingly greater fall speeds. In nature, a completely isolated graupel particle would soak up its meltwater and eventually transform into a raindrop (e.g., Rasmussen and Heymsfield 1987), thus preserving its mass and increasing its terminal fall speed. Partial filling was also tested, but it was found that using the full amount of melted ice to fill in voids gave the best match to a developmental scheme that predicts the amount of liquid water on ice (following Ferrier 1994).

REFERENCES

Avila, E. E., and R. G. Pereyra, 2000: Charge transfer during crystal-graupel collisions for two different cloud droplet size distributions. *Geophys. Res. Lett.,* **27,** 3837–3840.

——, G. M. Caranti, N. E. Castellano, and C. P. R. Saunders, 1998: Laboratory studies of the influence of cloud droplet size on charge transfer during crystal-graupel collisions. *J. Geophys. Res.,* **103** (D8), 8985–8996.

Beheng, K. D., 1992: A numerical study on the combined action of droplet coagulation, ice particle riming and the splintering process concerning maritime cumuli. *Beitr. Phys. Atmos.,* **55,** 201–214.

Brooks, I. M., C. P. R. Saunders, R. P. Mitzeva, and S. L. Peck, 1997: The effect on thunderstorm charging of the rate of rime accretion by graupel. *Atmos. Res.,* **43,** 277–295.

Bruning, E. C., W. D. Rust, T. J. Schuur, D. R. MacGorman, P. R. Krehbiel, and W. Rison, 2007: Electrical and polarimetric radar observations of a multicell storm in TELEX. *Mon. Wea. Rev.,* **135,** 2525–2544.

Carey, L. D., and K. M. Buffalo, 2007: Environmental control of cloud-to-ground lightning polarity in severe storms. *Mon. Wea. Rev.,* **135,** 1327–1353.

Connolly, P. J., T. W. Choularton, M. W. Gallagher, K. N. Bower, M. J. Flynn, and J. A. Whiteway, 2006: Cloud-resolving simulations of intense tropical Hector thunderstorms: Implications for aerosol–cloud interactions. *Quart. J. Roy. Meteor. Soc.,* **132,** 3079–3106, doi:10.1256/qj.05.86.

Cotton, W. R., G. J. Tripoli, R. M. Rauber, and E. A. Mulvihill, 1986: Numerical simulation of the effects of varying ice crystal nucleation rates and aggregation processes on orographic snowfall. *J. Climate Appl. Meteor.,* **25,** 1658–1680.

Deierling, W., and W. A. Petersen, 2008: Total lightning activity as an indicator of updraft characteristics. *J. Geophys. Res.,* **113,** D16210, doi:10.1029/2007JD009598.

Dendy, J. E., Jr., 1982: Black box multigrid. *J. Comput. Phys.,* **48,** 366–386.

Dye, J. E., and Coauthors, 1986: Early electrification and precipitation development in a small, isolated Montana cumulonimbus. *J. Geophys. Res.,* **91** (D1), 1231–1247.

Fan, J., R. Zhang, G. Li, and W.-K. Tao, 2007: Effects of aerosols and relative humidity on cumulus clouds. *J. Geophys. Res.,* **112,** D14204, doi:10.1029/2006JD008136.

——, and Coauthors, 2009: Dominant role by vertical wind shear in regulating aerosol effects on deep convective clouds. *J. Geophys. Res.,* **114,** D22206, doi:10.1029/2009JD012352.

Farley, R. D., 1987: Numerical modeling of hailstorms and hailstone growth. Part II: The role of low-density riming growth in hail production. *J. Climate Appl. Meteor.,* **26,** 234–254.

Ferrier, B. S., 1994: A double-moment multiple-phase four-class bulk ice scheme. Part I: Description. *J. Atmos. Sci.,* **51,** 249–280.

Hallett, J., and S. C. Mossop, 1974: Production of secondary ice particles during the riming process. *Nature,* **249,** 26–28.

Helsdon, J. H., Jr., W. A. Wojcik, and R. D. Farley, 2001: An examination of thunderstorm-charging mechanisms using a two-dimensional storm electrification model. *J. Geophys. Res.,* **106** (D1), 1165–1192.

——, S. Gattaleeradapan, R. D. Farley, and C. C. Waits, 2002: An examination of the convective charging hypothesis: Charge structure, electric fields, and Maxwell currents. *J. Geophys. Res.,* **107,** 4630, doi:10.1029/2001JD001495.

Heymsfield, A. J., and S. C. Mossop, 1984: Temperature dependence of secondary ice crystal production during soft hail growth by riming. *Quart. J. Roy. Meteor. Soc.,* **110,** 765–770.

Jiang, G.-S., and C.-W. Shu, 1996: Efficient implementation of weighted ENO schemes. *J. Comput. Phys.,* **126,** 202–228.

Khain, A., and A. Pokrovsky, 2004: Simulation of effects of atmospheric aerosols on deep turbulent convective clouds using a spectral microphysics mixed-phase cumulus cloud model. Part II: Sensitivity study. *J. Atmos. Sci.,* **61,** 2983–3001.

——, ——, and I. Sednev, 1999: Some effects of cloud–aerosol interaction on cloud microphysics structure and precipitation formation: Numerical experiments with a spectral microphysics cloud ensemble model. *Atmos. Res.,* **52,** 195–220.

——, D. Rosenfeld, and A. Pokrovsky, 2005: Aerosol impact on the dynamics and microphysics of deep convective clouds. *Quart. J. Roy. Meteor. Soc.,* **131,** 2639–2663.

——, N. Cohen, B. Lynn, and A. Pokrovsky, 2008: Possible aerosol effects on lightning activity and structure of hurricanes. *J. Atmos. Sci.,* **65,** 3652–3677.

——, V. Phillips, N. Benmoshe, and A. Pokrovsky, 2012: The role of small soluble aerosols in the microphysics of deep maritime clouds. *J. Atmos. Sci.,* **69,** 2787–2807.

Klemp, J. B., and R. B. Wilhelmson, 1978: Simulations of right- and left-moving storms produced through storm splitting. *J. Atmos. Sci.,* **35,** 1097–1110.

Konwar, M., R. S. Maheskumar, J. R. Kulkarni, E. Freud, B. N. Goswami, and D. Rosenfeld, 2012: Aerosol control on depth of warm rain in convective clouds. *J. Geophys. Res.,* **117,** D13204, doi:10.1029/2012JD017585.

Leighton, H. G., and R. R. Rogers, 1974: Droplet growth by condensation and coalescence in a strong updraft. *J. Atmos. Sci.,* **31,** 271–279.

Li, G., Y. Wang, and R. Zhang, 2008: Implementation of a two-moment bulk microphysics scheme to the WRF model to investigate aerosol-cloud interaction. *J. Geophys. Res.,* **113,** D15211, doi:10.1029/2007JD009361.

Lynn, B. H., A. P. Khain, J. Dudhia, D. Rosenfeld, A. Pokrovsky, and A. Seifert, 2005: Spectral (bin) microphysics coupled with a mesoscale model (MM5). Part II: Simulation of a CaPE rain event with a squall line. *Mon. Wea. Rev.,* **133,** 59–71.

Lyons, W. A., T. E. Nelson, E. R. Williams, J. A. Cramer, and T. R. Turner, 1998: Enhanced positive cloud-to-ground lightning in thunderstorms ingesting smoke from fires. *Science,* **282,** 77–80.

MacGorman, D. R., and Coauthors, 2008: TELEX: The Thunderstorm Electrification and Lightning Experiment. *Bull. Amer. Meteor. Soc.,* **89,** 997–1018.

——, I. R. Apostolakopoulos, N. R. Lund, N. W. S. Demetriades, M. J. Murphy, and P. Krehbiel, 2011: The timing of cloud-to-ground lightning relative to total lightning activity. *Mon. Wea. Rev.,* **139,** 3871–3886.

Macklin, W. C., 1962: The density and structure of ice formed by accretion. *Quart. J. Roy. Meteor. Soc.,* **88,** 30–50.

Mansell, E. R., 2010: On sedimentation and advection in multimoment bulk microphysics. *J. Atmos. Sci.,* **67,** 3084–3094.

——, D. R. MacGorman, C. L. Ziegler, and J. M. Straka, 2002: Simulated three-dimensional branched lightning in a numerical thunderstorm model. *J. Geophys. Res.,* **107** (D9), doi:10.1029/2000JD000244.

——, ——, ——, and ——, 2005: Charge structure and lightning sensitivity in a simulated multicell thunderstorm. *J. Geophys. Res.,* **110,** D12101, doi:10.1029/2004JD005287.

——, C. L. Ziegler, and E. C. Bruning, 2010: Simulated electrification of a small thunderstorm with two-moment bulk microphysics. *J. Atmos. Sci.,* **67,** 171–194.

Milbrandt, J. A., and H. Morrison, 2013: Predicting graupel density in a bulk microphysics scheme. *J. Atmos. Sci.,* **70,** 410–429.

Mitzeva, R. P., C. P. R. Saunders, and B. Tsenova, 2005: A modelling study of the effect of cloud saturation and particle growth rates on charge transfer in thunderstorm electrification. *Atmos. Res.,* **76,** 206–221, doi:10.1016/j.atmosres.2004.11.019.

——, ——, and ——, 2006: Parameterisation of non-inductive charging in thunderstorm regions free of cloud droplets. *Atmos. Res.,* **82,** 102–111, doi:10.1016/j.atmosres.2005.12.006.

Mossop, S. C., 1976: Production of secondary ice particles during the growth of graupel by riming. *Quart. J. Roy. Meteor. Soc.,* **102,** 25–44.

Moulton, J. D., J. E. Dendy Jr., and J. M. Hyman, 1998: The black box multigrid numerical homogenization algorithm. *J. Comput. Phys.,* **142,** 80–108.

Naccarato, K. P., O. Pinto Jr., and I. R. C. A. Pinto, 2003: Evidence of thermal and aerosol effects on the cloud-to-ground lightning density and polarity over large urban areas of Southeastern Brazil. *Geophys. Res. Lett.,* **30,** 1674, doi:10.1029/2003GL017496.

Orville, R. E., and Coauthors, 2001: Enhancement of cloud-to-ground lightning over Houston, Texas. *Geophys. Res. Lett.,* **28,** 2597–2600.

Petersen, W. A., H. J. Christian, and S. A. Rutledge, 2005: TRMM observations of the global relationship between ice water content and lightning. *Geophys. Res. Lett.,* **32,** L14819, doi:10.1029/2005GL023236.

Rasmussen, R. M., and A. J. Heymsfield, 1985: A generalized form for impact velocities used to determine graupel accretional densities. *J. Atmos. Sci.,* **42,** 2275–2279.

——, and ——, 1987: Melting and shedding of graupel and hail. Part I: Model physics. *J. Atmos. Sci.,* **44,** 2754–2763.

Reynolds, S. E., M. Brook, and M. F. Gourley, 1957: Thunderstorm charge separation. *J. Meteor.,* **14,** 426–436.

Rogers, R. R., and M. K. Yau, 1989: *A Short Course in Cloud Physics.* 3rd ed. Butterworth-Heinemann, 304 pp.

Rosenfeld, D., 1999: TRMM observed first direct evidence of smoke from forest fires inhibiting rainfall. *Geophys. Res. Lett.,* **26,** 3105–3108.

——, U. Lohmann, G. B. Raga, C. D. O'Dowd, M. Kulmala, S. Fuzzi, A. Reissell, and M. O. Andreae, 2008: Flood or drought: How do aerosols affect precipitation? *Science,* **321,** 1309–1313.

Saunders, C. P. R., and I. M. Brooks, 1992: The effects of high liquid water on thunderstorm charging. *J. Geophys. Res.,* **97** (D13), 14 671–14 676.

——, and S. L. Peck, 1998: Laboratory studies of the influence of the rime accretion rate on charge transfer during crystal/graupel collisions. *J. Geophys. Res.,* **103** (D12), 13 949–13 956.

Schultz, D. M., S. Mikkonen, A. Laaksonen, and M. B. Richman, 2007: Weekly precipitation cycles? Lack of evidence from United States surface stations. *Geophys. Res. Lett.,* **34,** L22815, doi:10.1029/2007GL031889.

Seifert, A., and K. D. Beheng, 2006: A two-moment cloud microphysics parameterization for mixed-phase clouds. Part 2: Maritime vs. continental deep convective storms. *Meteor. Atmos. Phys.,* **92,** 67–82, doi:10.1007/s00703-005-0113-3.

Shu, C.-W., 2003: High-order finite difference and finite volume WENO schemes and discontinuous Galerkin methods for CFD. *Int. J. Comput. Fluid Dyn.,* **17,** 107–118.

Steiger, S. M., and R. E. Orville, 2003: Cloud-to-ground lightning enhancement over southern Louisiana. *Geophys. Res. Lett.,* **30,** 1975, doi:10.1029/2003GL017923.

Storer, R. L., S. C. van den Heever, and G. L. Stephens, 2010: Modeling aerosol impacts on convective storms in different environments. *J. Atmos. Sci.,* **67,** 3904–3915.

Takahashi, T., 1976: Hail in an axisymmetric cloud model. *J. Atmos. Sci.,* **33,** 1579–1601.

——, 1978: Riming electrification as a charge generation mechanism in thunderstorms. *J. Atmos. Sci.,* **35,** 1536–1548.

——, 1983: Numerical simulation of winter cumulus electrification. Part I: Shallow cloud. *J. Atmos. Sci.,* **40,** 1257–1280.

——, 1984: Thunderstorm electrification—A numerical study. *J. Atmos. Sci.,* **41,** 2541–2558.

Tao, W.-K., J.-P. Chen, Z. Li, C. Wang, and C. Zhang, 2012: Impact of aerosols on convective clouds and precipitation. *Rev. Geophys.,* **50,** RG2001, doi:10.1029/2011RG000369.

van den Heever, S. C., and W. R. Cotton, 2007: Urban aerosol impacts on downwind convective storms. *J. Appl. Meteor. Climatol.,* **46,** 828–850.

Wang, C., 2005: A modeling study of the response of tropical deep convection to the increase of cloud condensation nuclei concentration: 1. Dynamics and microphysics. *J. Geophys. Res.,* **110,** D21211, doi:10.1029/2004JD005720.

Wicker, L. J., and R. B. Wilhelmson, 1995: Simulation and analysis of tornado development and decay within a three-dimensional supercell thunderstorm. *J. Atmos. Sci.,* **52,** 2675–2703.

——, and W. C. Skamarock, 2002: Time-splitting methods for elastic models using forward time schemes. *Mon. Wea. Rev.,* **130,** 2088–2097.

Wiens, K. C., S. A. Rutledge, and S. A. Tessendorf, 2005: The 29 June 2000 supercell observed during STEPS. Part II: Lightning and charge structure. *J. Atmos. Sci.,* **62,** 4151–4177.

Williams, E. R., and S. Stanfill, 2002: The physical origin of the land–ocean contrast in lightning activity. *C. R. Phys.,* **3,** 1277–1292.

——, and Coauthors, 2002: Contrasting convective regimes over the Amazon: Implications for cloud electrification. *J. Geophys. Res.,* **107,** 8082, doi:10.1029/2001JD000380.

Xu, J.-L., 1983: Hail growth in a three-dimensional cloud model. *J. Atmos. Sci.,* **40,** 185–203.

Yuan, T., L. A. Remer, K. E. Pickering, and H. Yu, 2011: Observational evidence of aerosol enhancement of lightning activity and convective invigoration. *Geophys. Res. Lett.,* **38,** L04701, doi:10.1029/2010GL046052.

——, and Coauthors, 2012: Aerosol indirect effect on tropospheric ozone via lightning. *J. Geophys. Res.,* **117,** D18213, doi:10.1029/2012JD017723.

Ziegler, C. L., 1985: Retrieval of thermal and microphysical variables in observed convective storms. Part I: Model development and preliminary testing. *J. Atmos. Sci.,* **42,** 1487–1509.

——, P. S. Ray, and N. C. Knight, 1983: Hail growth in an Oklahoma multicell storm. *J. Atmos. Sci.,* **40,** 1768–1791.

——, ——, and D. R. MacGorman, 1986: Relations of kinematics, microphysics and electrification in an isolated mountain thunderstorm. *J. Atmos. Sci.,* **43,** 2098–2114.

——, T. J. Lee, and R. A. Pielke Sr., 1997: Convective initiation at the dryline: A modeling study. *Mon. Wea. Rev.,* **125,** 1001–1026.